Published in final edited form as:
Nucl Instrum Methods Phys Res A. 2011 May 11; 638(1): 171–175. doi:10.1016/j.nima.2011.02.085.

Anti-contamination device for cryogenic soft X-ray diffraction microscopy

Xiaojing Huang[a,*], **Huijie Miao**[a], **Johanna Nelson**[a], **Joshua Turner**[a,1], **Jan Steinbrener**[a,2], **David Shapiro**[b,3], **Janos Kirz**[b], and **Chris Jacobsen**[a,c,d]

[a] Department of Physics and Astronomy, Stony Brook University, Stony Brook, NY 11794-3800, USA

[b] Advanced Light Source, Lawrence Berkeley National Laboratory, Berkeley, CA 94720, USA

[c] Department of Physics and Astronomy, Northwestern University, Evanston, IL 60208, USA

[d] Advanced Photon Source, Argonne National Laboratory, Argonne, IL 60439, USA

Abstract

Cryogenic microscopy allows one to view frozen hydrated biological and soft matter specimens with good structural preservation and a high degree of stability against radiation damage. We describe a liquid nitrogen-cooled anti-contamination device for cryogenic X-ray diffraction microscopy. The anti-contaminator greatly reduces the buildup of ice layers on the specimen due to condensation of residual water vapor in the experimental vacuum chamber. We show by coherent X-ray diffraction measurements that this leads to fivefold reduction of background scattering, which is important for far-field X-ray diffraction microscopy of biological specimens.

Keywords

X-ray Imaging; Cryogenic X-ray microscopy; Diffraction microscopy; Anti-contamination

1. Introduction

X-ray microscopy has been used for high resolution imaging of thick biological samples, because of its unique characteristics of short wavelength and deep penetration ability, which allow it to image samples beyond the thickness limit of electron microscopy [1–3]. Lens-based X-ray microscopy has been developed for imaging cryogenic biological samples in 2D and 3D with Fresnel zone plates [4–8]. This type of optics has a typical focussing efficiency of about 10% [9] and the achievable resolution is ultimately limited by the finest zone width. X-ray diffraction microscopy (XDM), also known as coherent diffraction imaging, was proposed by Sayre [10] as a novel imaging technique accomplished by illuminating an isolated object with a coherent X-ray beam and retrieving the image by numerically phasing the recorded far-field diffraction pattern using computational algorithms. This method is able to eliminate limitations imposed by X-ray optics [11], and has been widely applied since it was first demonstrated by Miao et al. [12]. The achieved

* Corresponding author. Current address: London Centre for Nanotechnology, University College, London WC1H 0AH, UK. Tel.: +44 630 252 0893. xiaojing.huang@ucl.ac.uk, xiaojinghuang@gmail.com (X. Huang)..
[1]Current address: Linac Coherent Light Source, SLAC National Accelerator Laboratory, Menlo Park, CA 94025, USA.
[2]Current address: Department of Biomolecular Mechanisms, Max Planck Institute for Medical Research, Jahnstr. 29, 69120 Heidelberg, Germany.
[3]Current address: National Synchrotron Light Source II, Brookhaven National Laboratory, Upton, NY 11973, USA.

resolution has been pushed down to 11213 nm for labeled features in biological samples [13].

A significant limitation of most biological applications of XDM [13–19] is that they have involved dried samples. Because water is the most abundant substance in biological samples, the dehydration process in sample preparation tends to cause structure artifacts. Furthermore, studies on electron [20,21] and X-ray [22,23] microcopes have shown that samples at cryogenic temperatures have a higher radiation damage tolerance to preserve structural information than those at room temperature. Thus, the frozen-hydrated state becomes a desired goal for imaging biological samples close to their natural state. The first XDM experimental on frozen-hydrated biological samples were successfully conducted recently [24,25].

In principle, a frozen-hydrated sample can be prepared by plunge-freezing the specimen into liquid ethane and maintaining it near liquid nitrogen temperature. During the sample preparation process, the cooling rate and sample temperature have to be carefully controlled to ensure that the liquid water forms thin and vitreous ice to satisfy the finite support constraint of XDM, which requires the object to be located in a compact area with no optical interaction outside. This means that the frozen hydrated specimen must be surrounded by a region of sufficiently smooth and vitrified ice, which has no crystalline structure and produces negligible diffuse scattering signal.

Since the sample grid is at very low temperature, the residual moisture in the experiment vacuum chamber tends to condense on the grid and form frost and ice crystals, which will violate the object isolation requirement and degrade the sample's diffraction pattern over time. Electron microscopy studies have shown that a cryogenic shield over the sample grid is important for imaging frozen samples [26].

We designed and installed an Anti-Contamination Device (ACD) for our cryogenic X-ray diffraction microscope [27], to reduce contamination buildup on the sample to a very low rate, which is an important step for enabling 2D and 3D data acquisition for far-field X-ray diffraction microscopy of biological specimens.

The mechanical design of the ACD will be described in Section 2. The thermal design and performance will be discussed in Section 3. The experimental diffraction results with X-rays will be shown in Section 4.

2. Mechanical design

2.1. Fitting cryo-sample holders

The X-ray diffraction microscope [27], located at beamline 9.0.1 at the Advanced Light Source, Lawrence Berkeley National Laboratory, uses Gatan 630 and 914 high-tilt cryo-specimen holders, which are motorized by a JEOL goniometer system with moving capability in *X*, *Y*, *Z*-directions and up to ±80 degree rotation around the *X*-axis. As shown in Fig. 1, the Gatan 630 holder uses rectangular grids with a 3 mm width, and the Gatan 914 holder uses the standard electron microscope circular grid with a 3 mm diameter, while the holder tip is about 2 mm wider than the grids. These holders are equipped with retractable slots to protect sample grids during the transfer process, but the grid is exposed to the residual gas during data aquisition.

To prevent the cryo-specimen from ice contamination due to water vapor in the residual gas, the anti-contaminator, a liquid nitrogen-cooled copper shield, is designed to surround the sample grid as close as possible with its temperature maintained at a level lower than that of the grid [21]. The anti-contaminator is made from copper, and coated with a thin layer of

gold, which protects the copper surface from oxidization and reduces the thermal emissivity of the surface. Its dimensions are determined by fitting the tips of both sample holders. To achieve maximum shielding of the sample, the anti-contaminator is designed as a hollow cylinder of 8 mm inner diameter that is inserted coaxially around the sample grid, as shown in Fig. 1. The inner surface of the anti-contaminator shielding is about 2.5 mm away from the edges of the sample grid and thus allows rotating the grid around the common axis for 3D data acquisition.

As the X-ray beam is perpendicular to the rotation axis of the sample holders, there are two 4 mm diameter windows opened on the side wall of the anti-contaminator, which allow the X-ray beam to illuminate the sample grid and the diffraction signal to propagate without being obstructed.

2.2. Mounting and positioning

The anti-contaminator is mounted on a Micos VT-21 stepper motor stage (shown in Fig. 2), which gives 26 mm travel ranges in both directions with 0.5 μm accuracy. The adjustment ability in *X*- and *Y*-directions helps align the anti-contaminator with the rotation axis of the grid, and align the 4 mm diameter side windows with the opening area of the grid as well. The anti-contaminator can also be fully removed from the grid in the *X*-direction, when it is not in use. A motor in the *Z*-direction is not required, because the *X*–*Y* stage mounting slot on the chamber is well matched with the goniometer system in the *Z*-direction.

3. Thermal design

The water molecules on sample grids can be rearranged to form cubic ice crystal structure by warming up vitreous ice, or by residual water vapor depositing onto the grid surface at a temperature between approximately 140 and 145 K [28]. Based on both of these considerations, the sample grid is usually maintained below 133 K during data acquisition. In our experiments, we normally keep the sample grid temperature lower than 113 K.

To keep the ACD functioning properly, it is crucial that it is cooled and maintained at a temperature lower than the cryogenic sample grid. We now consider what cooling power is required to keep the ACD operating at about 103 K.

3.1. Cooling path and thermal isolation

The cooling power is provided by a cooling path, which consists of a liquid nitrogen dewar, a copper rod and a copper braid.

A customized liquid nitrogen dewar functions as a heat sink on the top of the microscope chamber as shown in Fig. 3, and it canhold temperature for 4 h after each refill. The dewar has a hollow aluminum “tail” at the bottom, which is filled with liquid nitrogen and connects to the inside of the chamber through a flange. From there the cooling path is extended close to the sample grid via a 22 cm long, 1.27 cm diameter, solid copper rod, which is bent to fit the chamber. The copper rod is bolted firmly to the tail of the dewar with an indium foil sealing the joint interface to provide better thermal conductivity.

The other end of this copper rod is about 1.27 cm away from the anti-contaminator. They are connected using a 5 cm long copper braid (not shown in Fig. 3). The maximum traveling range of the ACD motor stage is $\sqrt{2} \cdot 26 \quad \text{mm}$ (~3.7 cm). The 5cm copper braid provides the necessary flexibility between the fixed copper rod and the movable anti-contaminator.

The anti-contaminator is cooled by liquid nitrogen, while the motor stage is at room temperature. To minimize conductive heat exchange between the cold anti-contaminator and

the warm motor stage, a low thermal conductivity fiberglass support is used to mount the ACD to the motor stage. This support is also hollow to reduce the effective thermal conduction cross-section. It is 30 mm long with 10 mm outer and 5 mm inner diameter, as shown in Fig. 2.

3.2. Heating power

The heating power, which warms the ACD, is mainly from two sources: one is the thermal radiation power P_{rad}, from the warm vacuum chambertothe cold anti-contaminatoraswellasother parts of the cooling path; the other is the thermal conduction power P_{cond} from the warm motor stage to the anti-contaminator.

Suppose that the copper rod is at a temperature (~ 77 K) close to liquid nitrogen at the side attached to the dewar. In order to achieve the desired temperature of 103 K on the anti-contaminator, we allow a temperature drop of about 10 degrees through the copper rod, and another 15 degree drop through the copper braid, including the effect of the connections.

3.2.1. Thermal radiation power—To estimate the thermal radiation power P_{rad}, we model the anti-contaminator as a 35 mm long, hollow copper cylinder with 10 mm outer diameter and 8 mm inner diameter. When the anti-contaminator works at 103 K and the chamber is at room temperature 293 K, the heat transfer power through thermal radiation from the chamber to the anti-contaminator can be calculated [29] as

$$P_{\text{rad}}=\varepsilon\sigma A_s\left(T_{\text{c}}^4-T_{\text{a}}^4\right) \tag{1}$$

where ε is the emissivity of gold (about 0.02), σ is the Stefan–Boltzmann constant 5.67×10^{-8} W/(m^2 × K^4), A_s is the outer surface area of the hollow cylinder 1.1×10^{-3} m^2, T_c and T_a are temperatures in Kelvin of the chamber and the anti-contaminator, 293 and 103 K, respectively. Substituting the numbers into Eq. (1), we obtain P_{rad_1} to be approximately 9 mW.

Both the copper rod and copper braid are coated with gold. The thermal radiation powers between the vacuum chamber and the copper rod P_{rad_2}, and between the vacuum chamber and the copper braid P_{rad_3}, can also be calculated using Eq. (1) to be 73 and 63 mW, respectively. Then the total heating power through thermal radiation P_{rad} equals P_{rad_1} + P_{rad_2} + P_{rad_3} = 145 mW.

3.2.2. Thermal conduction power—One side of the fiber glass support is connected to the anti-contaminator at 103 K, while the other side is connected to the warm stainless steel support which is attached to the motor stage at room temperature 293 K. The heat transfer power through thermal conduction P_{cond} from the motor stage to the anti-contaminator can be calculated [29] as

$$P_{\text{cond}}=\frac{kA_c\Delta T}{\Delta l} \tag{2}$$

where k is the thermal conductivity of fiber glass 0.05 W/(m × K), A_c is the cross-section area 5.9×10^{-5} m^2, ΔT is the temperature difference between the two ends 190 K, and Δl is the length of the conduction path 0.03 m. We obtain that P_{cond} is about 19 mW through this fiber glass support.

3.2.3. Other heating powers—With a pressure below 10^{-6} torr, which is typical for cryogenic soft X-ray diffraction microscope, the heat transfer power through convection is negligible compared to radiation and conduction [29].

With a typical beam flux of 10^9 incident photons per second for the X-ray diffraction microscope operated at 520 eV, the beam heating power by full absorption is also negligible (~ 10^{-5} mW).

3.3. Cooling power estimate

The cooling power P'_{rod} that the copper rod is able to provide can be estimated by Eq. (2). With k = 500 W/(m × K) for copper, $A_c = 1.27 \times 10^{-4}$ m^2, ΔT = 10 K, and Δl = 0.22 m, P'_{rod} is about 2.9 W.

The copper braid contains 384 wires, each of which is of type AWG 36 or 127 μm in diameter. Supposing that the temperature drops 15 K across the copper braid, the temperature on the anti-contaminator side of the braid is around 103 K. The cooling power of the copper braid P'_{braid} can then be estimated to be 729 mW using Eq. (2).

As we can see, the cooling power that the cooling path is able to provide (P'_{rod} or P'_{braid}) is much greater than the heating power P_{rad}+P_{cond}.

3.4. Temperature measurement

To monitor how the ACD cools down, three silicon diode temperature sensors were mounted on the cooling path: the first sensor near the connection interface between the dewar tail and the copper rod, the second one at the end of the copper rod away from the dewar, and the third sensor on the anti-contaminator.

The system was tested with the microscope chamber pumped down to 10^{-7} torr and the liquid nitrogen dewar filled with liquid nitrogen. When the temperatures stabilized, the readings were 78, 85, and 101 K, respectively. This indicates that the ACD cools well as expected.

We also note that although the designed cooling power is much higher than the required amount, the achieved temperature is not remarkably better than the designed goal. This implies that the thermal connection is not perfect for the cooling path. Especially at the joints, the clamping mechanism results in thermal barriers, even with indium foil being used to improve the thermal contact.

4. Diffraction experiment data

The ACD performance was tested by monitoring changes in the diffraction pattern from blank formvar grids at cryogenic temperature across a time span comparable to 2D and 3D data acquisitions (typically minutes to hour for 2D and 10 h for 3D [18,30]). Comparing the experimental data without ACD (Section 4.1) and with ACD (Section 4.2), we conclude that the ACD functions as expected.

4.1. Test without ACD

Moisture condensation process was tested with Gatan 630 holder before the ACD was installed [31]. A room temperature grid was inserted through an air lock into the microscope's vacuum chamber. It was cooled down in the chamber with the retractable slot covered till its temperature stabilized at 113 K. The grid was then uncovered, and diffraction

patterns were recorded from an initially blank area, when the pressure was about 3×10^{-6} torr. The data were taken with 520 eV X-rays. The azimuthally averaged diffraction intensities of the initial diffraction image along with a second one taken an hour later at the same spot are shown as solid and dashed black lines in Fig. 4, both of which are higher than dark noise signal by a factor of 2. The azimuthal averaging process smooths out the sharp variations due to individual speckles to reveal the average power scattered as a function of spatial frequency. The overall diffraction intensity is dramatically increased in this one-hour interval, and a ring of scattering signal was observedaroundaspatialfrequency of 12 mm ^{1} (inset image of Fig. 4). This fivefold diffraction intensity increment compared with initial data indicates that the scattering is dominated by this particular range of randomly oriented volume gratings. The result implies that without the ACD, significant moisture condensation and ice formation occurred on the cryogenic test grid within 1 h.

4.2. Test with ACD

The ice testing experiment was performed second time with Gatan 914 holder after the ACD was installed in the cryogenic X-ray diffraction microscope. The pressure was observed to drop by one order of magnitude when the ACD was cooled.

This test grid was prepared following the frozen-hydrated sample preparation steps on a formvar-coated grid except that distilled water was used instead of biological sample solution. The cold grid was then transferred into the microscope vacuum chamber, where it was maintained at 113 K. With the ACD cold, the chamber pressure stabilized at 5×10^{-8} torr. Diffraction data from a clean spot were taken with 520 eV X-rays after the grid temperature was stable, and again 16 h later. The azimuthally averaged diffraction intensity curves are shown as blue lines in Fig. 4. All of them are at least two-fold stronger than dark noise signal. The blue solid and fine-dashed lines in Fig. 4 show that after 16 h the diffraction intensity increased almost uniformly and smoothly for most spatial frequencies. Assuming a linear increase of the condensation of moisture with time, we can calculate the expected power spectrum after 1 h. This is plotted as the blue coarse-dashed line in Fig. 4, which gives slightly higher (5%) diffraction intensities than the initial power spectrum, while the diffraction signal increased five times in the same time interval without ACD.

Note that this grid was plunge-frozen and kept in liquid nitrogen before it was transferred into the microscope chamber. The ice thickness on this grid is therefore larger than on the previous grid used for testing ice accumulation without the ACD. It also possibly experienced exposures to the atmosphere environment during the preparation and transfer processes. These facts can explain why the total initial scattered power of the grid tested with the ACD (the blue solid line in Fig. 4) is higher than that without the ACD (the black solid line in Fig. 4). We also found a minor leakage around the sealing o-ring of Gatan 914 holder in our experiment [32]. This could be another reason for the higher initial scattering signal for blue curves.

5. Conclusion

We designed and installed an Anti-Contamination Device that mitigates the moisture condensation and ice structure formation problem for a cryogenic X-ray diffraction microscope. The ACD is cooled by liquid nitrogen to achieve a working temperature of around 103 K. The experimental data show that the ACD significantly slows down moisture accumulation and amorphous ice formation up to 16 h. It also improves the vacuum by an order of magnitude. All these functions are crucial for cryo-XDM, and enable the possibility of 2D and 3D data acquisition from cryogenic specimens.

Acknowledgments

We thank the Division of Materials Sciences and Engineering, Office of Basic Energy Sciences, at the Department of Energy for support of X-ray diffraction microscopy methods and instrumentation development under contract DE-FG02-07ER46128. We also thank the National Institute for General Medical Services at the National Institutes for Health for support of the application of this method to biological imaging under contract 5R21EB6134. The Advanced Light Source is supported by the Director, Office of Science, Office of Basic Energy Sciences, of the U.S. Department of Energy under Contract No. DE-AC02-05CH11231. Finally, we thank Stefano Marchesini and George Meigs of ALS for the fruitful discussions related to this project, and Richard Celestre and Tony Warwick of ALS for help and advice.

References

1. Sayre D, Kirz J, Feder R, Kim DM, Spiller E. Science. 1977; 196:1339. [PubMed: 867033]
2. Grimm R, Bärmann M, Häckl W, Typke D, Sackman E, Baumeister W. Biophysical Journal. 1997; 72:482. [PubMed: 8994635]
3. Jacobsen, C.; Medenwaldt, R.; Williams, S. A perspective on biological X-ray and electron microscopy. In: Thieme, J.; Schmahl, G.; Umbach, E.; Rudolph, D., editors. X-ray Microscopy and Spectromicroscopy. Springer-Verlag; Berlin: 1998. p. II93-II102.
4. Wang Y, Jacobsen C, Maser J, Osanna A. Journal of Microscopy. 2000; 197(1):80. [PubMed: 10620151]
5. Weiß D, Schneider G, Niemann B, Guttmann P, Rudolph D, Schmahl G. Ultramicroscopy. 2000; 84(3–4):185. [PubMed: 10945329]
6. Schneider G, Anderson E, Vogt S, Knöchel C, Weiss D, Legros M, Larabell C. Surface Review and Letters. 2002; 9(1):177.
7. Larabell CA, Le Gros MA. Molecular Biology of the Cell. 2004; 15:957. [PubMed: 14699066]
8. Parkinson DY, McDermott G, Etkin LD, Le Gros MA, Larabell CA. Journal of Structural Biology. 2008; 162:380. [PubMed: 18387313]
9. Kirz J. Journal of the Optical Society of America. 1974; 64:301.
10. Sayre, D. Prospects for long-wavelength X-ray microscopy and diffraction. In: Schlenker, M., editor. Imaging Processes and Coherence in Physics. Springer-Verlag; Berlin: 1980. p. 229
11. Huang X, Miao H, Steinbrener J, Nelson J, Stewart A, Shapiro D, Turner J, Jacobsen C. Optics Express. 2009; 17:13541. [PubMed: 19654762]
12. Miao J, Charalambous P, Kirz J, Sayre D. Nature. 1999; 400:342.
13. Nelson J, Huang X, Steinbrener J, Shapiro D, Kirz J, Marchesini S, Neiman AM, Turner J, Jacobsen C. Proceedings of the National Academy of Sciences. 2010; 107:7235.
14. Miao J, Hodgson KO, Ishikawa T, Larabell CA, LeGros MA, Nishino Y. Proceedings of the National Academy of Sciences. 2003; 100:110.
15. Shapiro D, Thibault P, Beetz T, Elser V, Howells M, Jacobsen C, Kirz J, Lima E, Miao H, Neiman AM, Sayre D. Proceedings of the National Academy of Science. 2005; 102(43):15343.
16. Song C, Jiang H, Mancuso A, Amirbekian B, Peng L, Sun R, Shah SS, Hong Zhou Z, Ishikawa T, Miao J. Physical Review Letters. 2008; 101(15):12.
17. Williams GJ, Hanssen E, Peele AG, Pfeifer MA, Clark J, Abbey B, Cadenazzi G, de Jonge MD, Vogt S, Tilley L, Nugent KA. Cytometry Part A. 2008; 73A(10):949.
18. Nishino Y, Takahashi Y, Imamoto N, Ishikawa T, Maeshima K. Physical Review Letters. 2009; 102(1)
19. Jiang H, Song C, Chen C, Xu R, Raines K, Fahimian B, Lu C, Lee T, Nakashima A, Urano J, Ishikawa T, Tamanoi F, Miao J. Proceedings of the National Academy of Sciences. 2010; 107:11234.
20. Glaeser RM, Taylor KA. Journal of Microscopy. 1978; 112:127. [PubMed: 347079]
21. Steinbrecht, RA.; Zierold, K., editors. Cryotechniques in Biological Electron Microscopy. Springer-Verlag; Berlin: 1987.
22. Schneider G. Ultramicroscopy. 1998; 75:85. [PubMed: 9836467]

23. Maser J, Osanna A, Wang Y, Jacobsen C, Kirz J, Spector S, Winn B, Tennant D. Journal of Microscopy. 2000; 197(1):68. [PubMed: 10620150]
24. Huang X, Nelson J, Kirz J, Lima E, Marchesini S, Miao H, Neiman A, Shapiro D, Steinbrener J, Stewart A, Turner J, Jacobsen C. Physical Review Letters. 2009; 103(19):198101. [PubMed: 20365955]
25. Lima E, Wiegart L, Pernot P, Howells M, Timmins J, Zontone F, Madsen A. Physical Review Letters. 2009; 103(19):198102. [PubMed: 20365956]
26. Cheng A, Fellmann D, Pulokas J, Potter CS, Carragher B. Journal of Structural Biology. 2006; 154(3):303. [PubMed: 16632377]
27. Beetz T, Howells MR, Jacobsen C, Kao C-C, Kirz J, Lima E, Mentes TO, Miao H, Sanchez-Hanke C, Sayre D, Shapiro D. Nuclear Instruments and Methods in Physics Research A. 2005; 545(1–2): 459.
28. Dubochet, J.; Adrian, M.; Chang, JJ.; Lepault, J.; McDowall, AW. Cryoelectron microscopy of vitrified specimens. In: Steinbrecht, RA.; Zierold, K., editors. Cryotechniques in Biological Electron Microscopy. Springer-Verlag; Berlin: 1987. p. 114-131.
29. Barron, RF. Cryogenic Heat Transfer. Taylor & Francis; 1999.
30. Chapman HN, Barty A, Marchesini S, Noy A, Hau-Riege SP, Cui C, Howells MR, Rosen R, He H, Spence JCH, Weierstall U, Beetz T, Jacobsen C, Shapiro D. Journal of the Optical Society of America A. 2006; 23:1179.
31. Miao H, Downing K, Huang X, Kirz J, Marchesini S, Nelson J, Shapiro D, Steinbrener J, Stewart A. 2009; 186:012055.Journal of Physics: Conference Series
32. Nelson, J. Ph.D. Thesis. Department of Physics and Astronomy, Stony Brook University; 2010. X-ray diffraction microscopy on frozen hydrated specimens..

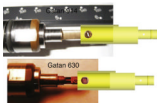

Fig. 1.
Gatan 914 cryo-sample holder uses 3 mm diameter round grids, and Gatan 630 holder uses rectangular grids with a width of 3 mm. The anti-contaminator coaxially fits both holders. There are two holes on its side wall, which allow the X-ray beam to illuminate the sample grid and the diffraction signal to propagate without being obstructed.

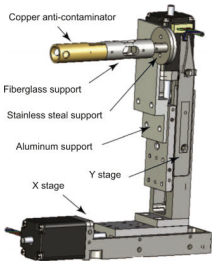

Fig. 2.

The anti-contaminator is a hollow copper rod coated with gold. It is mounted on a Micos VT-21 stepper motor stage. The ACD is thermally isolated from the warm stage by a hollow fiberglass support and a stainless steel support.

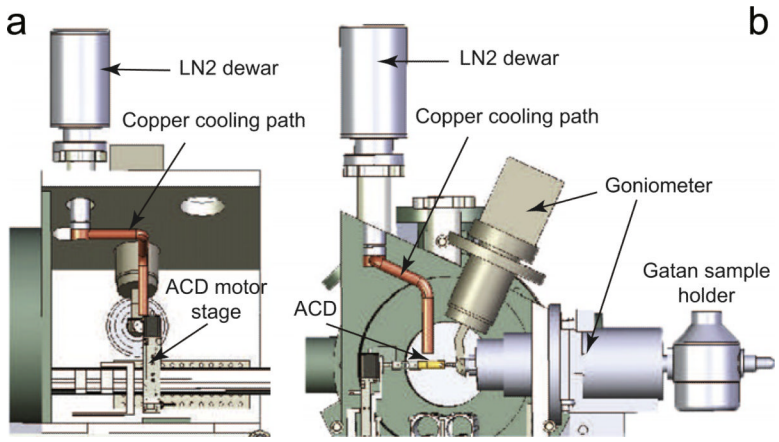

Fig. 3.

The anti-contaminator is cooled by a liquid nitrogen dewar, which is mounted on the top of the microscope chamber. A copper rod attached to the dewar bottom is bent to fit the chamber and extends to about 1.27 cm away from the anti-contaminator. The tail of the copper rod is connected to the ACD by a 5 cm long, 1.27 cm wide copper braid (not shown in the figure). (a) The side view of the chamber with cooling path. (b) The cross-section view along X-ray direction.

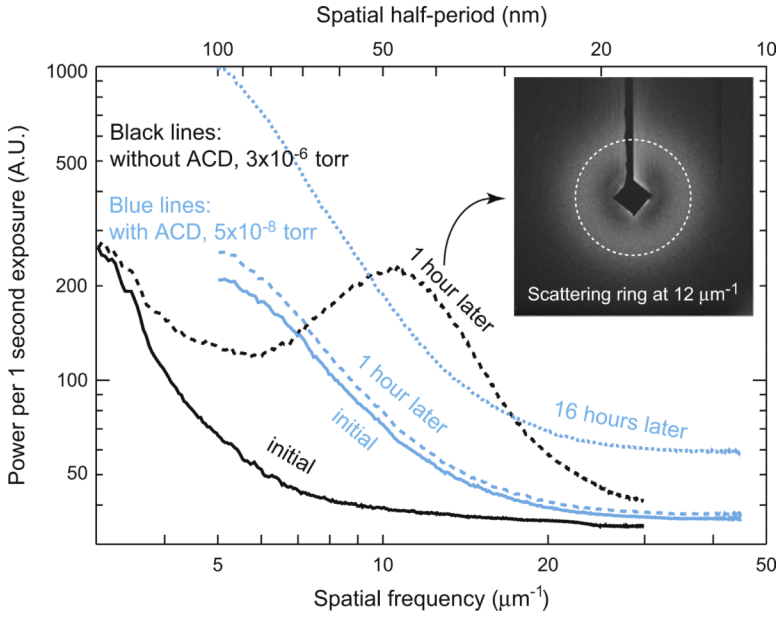

Fig. 4.

The azimuthally averaged curves of diffraction patterns. Black lines, measured with Gatan 630 holder and without ACD at the beginning (black solid) and 60 min later (black dashed). Blue lines, measured with Gatan 914 holder and with ACD at the beginning (blue solid), 60 min later (blue dashed) and 16 h later (blue fine-dashed). The vacuum pressure is improved by ACD. The ACD reduces moisture condensation and amorphous ice formation for up to 16 h. The inset image is the diffraction pattern taken 1 h later without ACD. A ring of scattering signal was observed around a spatial frequency of 12 μm^{-1}. (For interpretation of the references to color in this figure legend, the reader is referred to the web version of this article.)